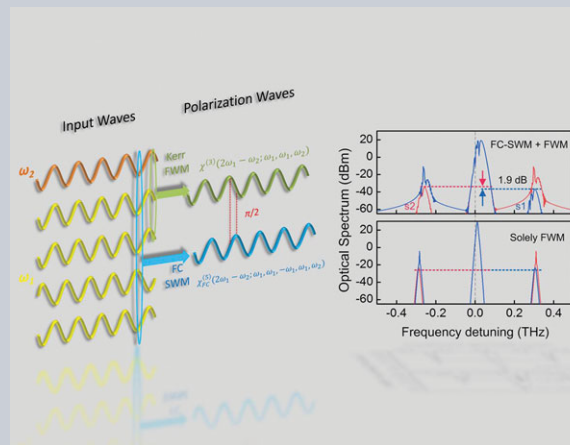


Abstract Nonlinear wave mixing in mesoscopic silicon structures is a fundamental nonlinear process with broad impact and applications. Silicon nanowire waveguides, in particular, have large third-order Kerr nonlinearity, enabling salient and abundant four-wave-mixing dynamics and functionalities. Besides the Kerr effect, in silicon waveguides two-photon absorption generates high free-carrier densities, with corresponding fifth-order nonlinearity in the forms of free-carrier dispersion and free-carrier absorption. However, whether these fifth-order free-carrier nonlinear effects can lead to six-wave-mixing dynamics still remains an open question until now. Here we report the demonstration of free-carrier-induced six-wave mixing in silicon nanowires. Unique features, including inverse detuning dependence of six-wave-mixing efficiency and its higher sensitivity to pump power, are originally observed and verified by analytical prediction and numerical modeling. Additionally, asymmetric sideband generation is observed for different laser detunings, resulting from the phase-sensitive interactions between free-carrier six-wave-mixing and Kerr four-

wave-mixing dynamics. These discoveries provide a new path for nonlinear multi-wave interactions in nanoscale platforms.



Six-wave mixing induced by free-carrier plasma in silicon nanowire waveguides

Heng Zhou^{1,*}, Mingle Liao¹, Shu-Wei Huang², Linjie Zhou³, Kun Qiu¹, and Chee Wei Wong^{2,*}

1. Introduction

Silicon solid-state nanophotonic structures have a large third-order Kerr nonlinearity and strong light confinement, enabling nonlinear optical dynamics with broad impact and applications. Four-wave mixing (FWM), as an elemental nonlinear process, has been deeply investigated in nanoscale silicon platforms [1]–[5] and implemented in a multitude of functionalities, ranging from optical signal regeneration [6], mid-infrared frequency conversion [7], [8], phase conjugation [9], continuum generation [10], regenerative oscillations [11], correlated photon generation [12], and spectroscopy [13]. Essentially, FWM arises when two intense laser fields cause oscillation of the refractive index via the Kerr effect, which in turn imposes nonlinear phase modulation back onto the input driving fields themselves, producing modulation sidebands at new frequencies that satisfy photon energy and momentum conservation conditions [14], [15]. In silicon nonlinear waveguides, in addition to the Kerr effect, two-photon absorption (TPA) generates considerable free-carrier densities, with corresponding nonlinearity and change of refractive index via free-carrier dispersion (FCD) and free-carrier absorption (FCA) [14]. Importantly, the generation of free-carrier den-

sity via TPA is already quadratically proportional to the incident laser intensity, making the cascaded refractive-index modulation via FCA/FCD a fifth-order nonlinear dynamics on top of the third-order Kerr nonlinearity [16]–[24]. Various FCD/FCA-induced nonlinear phenomena have been demonstrated in silicon, such as soliton fission [18], [19], soliton compression [20], frequency shift [21], and spectrum broadening [23], [24]. However, a fundamentally important question—akin to the third-order Kerr effect generating FWM, whether the fifth-order FCD/FCA can give rise to six-wave-mixing dynamics—has not been probed until now.

Here we present the demonstration of free-carrier-induced six-wave mixing (FC-SWM) in silicon waveguides. We show a non-dispersion-induced inverse dependence of the FC-SWM strength on input laser detunings, which confirms the existence of FC-SWM resulting in the predominance of FC-SWM over FWM at small laser detunings. Furthermore, we map out the stronger dependence of FC-SWM on input pump power compared to conventional Kerr FWM. Finally, we observe asymmetric sideband generation efficiencies and identify the phase-sensitive interaction between FC-SWM and FWM as the mechanism for such symmetry breaking.

¹ Key Lab of Optical Fiber Sensing and Communication Networks, University of Electronic Science and Technology of China, Chengdu, 611731, China

² Mesoscopic Optics and Quantum Electronics Laboratory, University of California, Los Angeles, CA 90095, USA

³ State Key Laboratory of Advanced Optical Communication Systems and Networks, Shanghai Jiao Tong University, Shanghai, 200240, China

*Corresponding author: e-mail: zhouheng@uestc.edu.cn; cheewei.wong@ucla.edu

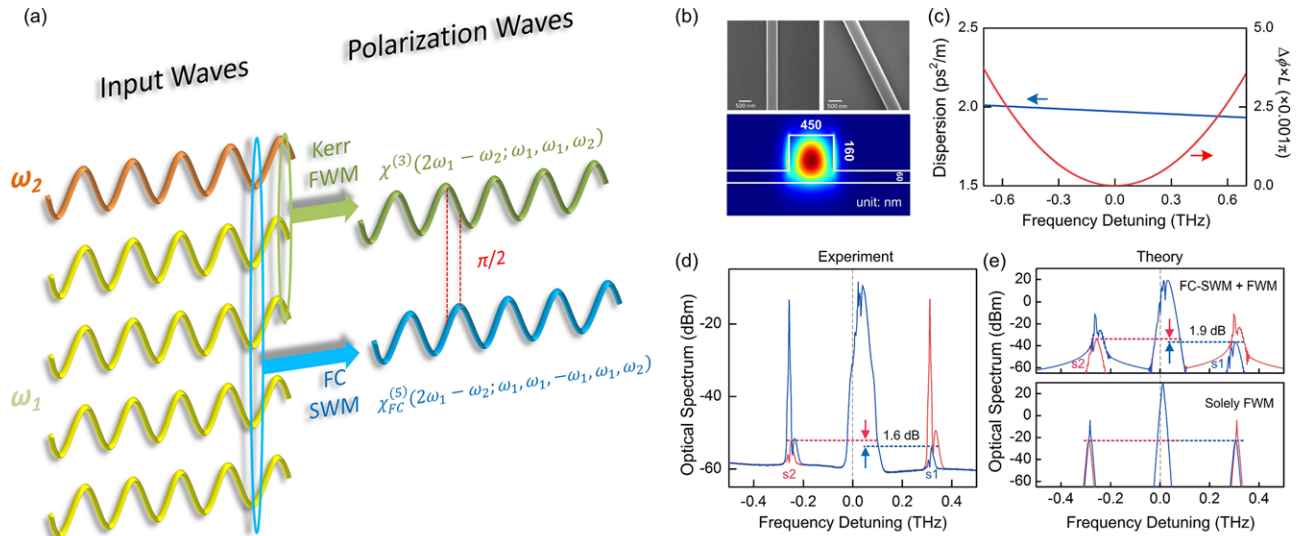


Figure 1 Six-wave-mixing spectra and nanowire characteristics. (a) The origin of Kerr FWM and FC-SWM in silicon nanowire waveguide with two input laser frequencies. (b) Scanning electron micrographs of the measured nanowire (upper panel) and simulated mode profile of the fundamental TE₁₁ mode using finite-difference time-domain-based mode solver (lower panel). (c) Nanowire dispersion of the TE₁₁ mode (left y-axis) and the corresponding linear phase mismatch (right y-axis). (d) Measured wave-mixing spectra with 0.28 THz detuning, and the generated sideband idler powers at smaller (s1) and bigger (s2) frequencies. (e) Numerically simulated wave-mixing spectra using the NLSE model with experimental parameters, for the case of solely FWM (lower) and Drude FC-SWM plus FWM (upper). The spectrum power discrepancies between numerical and experimental results are due to the fact that the experimental pulse powers were averaged by the 50 MHz pulse repetition rate.

2. Concept and theoretical analysis

Kerr and free-carrier nonlinear dynamics in silicon can be described by the nonlinear Schrödinger equation (NLSE), which when coupled with the free-carrier generation and recombination dynamics are governed by [14]

$$\frac{\partial E}{\partial z} = -i\frac{\beta_2}{2}\frac{\partial^2 E}{\partial t^2} + \frac{\beta_3}{6}\frac{\partial^3 E}{\partial t^3} - \frac{\alpha_l}{2}E + (i\gamma - \frac{\beta_{\text{TPA}}}{2A_0})|E|^2E - (i\delta + \sigma)N_cE, \quad (1)$$

$$N_c = \int_0^t \left(\frac{\beta_{\text{TPA}}}{2A_0^2 h\nu_0} |E(z, \tau)|^4 - \frac{N_c}{\tau_c} \right) d\tau. \quad (2)$$

In Eqs. (1) and (2), E is the slowly varying envelope of the overall input fields into the nanowire waveguide, β_n is the n th-order dispersion, γ is the effective Kerr nonlinear coefficient, β_{TPA} is the degenerate TPA coefficient, N_c is the free-carrier density, δ and σ are the Drude FCD and FCA coefficients, respectively, A_0 denotes the effective mode area, τ_c is the free-carrier lifetime, h is Planck's constant, and ν_0 is the pump frequency. To analytically derive the wave-mixing process, the input light field E is described by $A_1 \cos(\omega_1 t) + A_2 \cos(\omega_2 t)$. As shown in Fig. 1(a), here we utilize two input laser frequencies to study the degenerate FWM via $\chi^{(3)}(2\omega_1 - \omega_2; \omega_1, \omega_1, \omega_2)$ and the degenerate FC-SWM via $\chi_{\text{FC}}^{(5)}(2\omega_1 - \omega_2; \omega_1, \omega_1, -\omega_1, \omega_1, \omega_2)$. Such two-frequency configuration can greatly reduce the

complexity of theoretical derivation without loss of generality (more discussions detailed in Supporting Information [25]). Meanwhile, it should be noted that $\chi_{\text{FC}}^{(5)}$ is induced by FCD/FCA, and has no contribution from the fifth-order electronic nonlinearity n_4 [14]. Considering the evolution of the input field and neglecting the dispersion of the waveguide, the nonlinear wave-mixing strength (NM) experienced by the input field E can be written as (detailed derivation in Supporting Information [25])

$$NM = \exp\left(iG \cos(bt) + \frac{iD}{b} \sin(bt)\right) \times (1 + P \cos(bt)) \times \left(1 + \frac{A}{b} \sin(bt)\right). \quad (3)$$

Here $b = \omega_1 - \omega_2$ is the frequency detuning between input lasers, $P = -LA_1 A_2 \beta_{\text{TPA}} (2A_0)^{-1}$, $G = LA_1 A_2 \gamma$, $A = D\sigma\delta^{-1}$, $D = -3LA_1^3 A_2 \delta \beta_{\text{TPA}} (4A_0^2 h\nu_0)^{-1}$, and L is the waveguide length. Herein G , P , D , and A represent the effects of Kerr, TPA, FCD, and FCA, respectively. In our study we consider that TPA, FCA, and FCD respond instantaneously to the beating oscillation corresponding to the input laser detunings tested in the experiments ($b/2\pi < 1$ THz) [26]. Importantly, Eq. (3) shows that the Kerr and FCD effects cause nonlinear phase modulations that have a $\pi/2$ phase offset with respect to each other (the first and second terms on the right-hand side of Eq. (3), respectively), while TPA and FCA cause nonlinear intensity modulations that also have a $\pi/2$ phase offset (the third and fourth terms on

the right-hand side of Eq. (3), respectively). Furthermore, Eq. (3) can be re-written as

$$NM = \exp(iH \sin(bt + \theta)) \times (1 + M \cos(bt + \psi)). \quad (4)$$

Therein, $H = \sqrt{(D/b^2) + G^2}$, $M = \sqrt{(A/b)^2 + P^2}$, $\theta = \arctan(Gb/D)$, $\pi/2 \leq \theta < \pi$, and $\psi = \arctan(-A/Pb)$, $\pi/2 \leq \psi < \pi$. The values of θ and ψ are determined by the signs of G , P , D , and A . Using the Bessel expansion, we thus arrive at

$$NM = \sum_{n=-1}^1 J_n(H) e^{inbt+in\theta} \times \left(1 + \frac{1}{2} M (e^{ibt+i\psi} + e^{-ibt-i\psi}) \right). \quad (5)$$

In Eq. (5), J_n is the n th-order Bessel function. Simplifying Eq. (5) with frequency detunings $\pm b$, respectively, we finally obtain [25]

$$NM_b = \frac{1}{2} M J_0 e^{i\psi} + J_1 e^{i\theta}, \quad (6)$$

$$NM_{-b} = \frac{1}{2} M J_0 e^{-i\psi} - J_1 e^{-i\theta}. \quad (7)$$

First, as seen in Eq. (5) and the expressions of H and M , the FC-SWM components induced by FCD and FCA have an inverse dependence on the input laser detuning ($1/b$), while FWM from Kerr and TPA is detuning independent. Second, the effective fifth-order FC-SWM components are proportional to $A_1^3 A_2$ (seen in the expressions of D and A), while the third-order FWM components are only proportional to $A_1 A_2$ (seen in the expressions of G and P), implying that FC-SWM has a higher sensitivity than FWM. Third, comparing Eqs. (6) and (7), under the combinational effects of Kerr, TPA, FCA, and FCD in silicon, the generated overall wave-mixing sideband power ($|NM_{\pm b}|^2$) can be asymmetric for positive and negative input laser detunings, even when the waveguide dispersion is neglected. The exact extent of the asymmetry depends on the parameters of the measured waveguide and input light fields. We next present detailed FC-SWM and FWM measurements to demonstrate and validate these theoretical predications.

3. Experimental results and discussion

We study a 0.3-mm-long rib silicon nanowire fabricated on a silicon-on-insulator wafer, with the scanning electron micrograph shown in Fig. 1(b). Its numerically estimated mode profile and corresponding dispersion of the fundamental TE₁₁ mode are shown in Fig. 1(c). The measured nanowire waveguide has a linear loss $\alpha_1 = 2$ dB/cm, with an effective mode area $A_0 = 1.3 \times 10^{-13}$ m², a degenerate TPA coefficient $\beta_{\text{TPA}} = 9 \times 10^{-12}$ m/W, a FCA coefficient

$\theta = 1.45 \times 10^{-21}$ m², a FCD coefficient $\delta = 1.0 \times 10^{20}$ m², and a free-carrier recombination lifetime $\tau_c = 500$ ps [14], [21], [22]. The two incident drive lasers consist of a 50 MHz repetition rate, 100 ps pulse width pump field (amplitude A_1 and central angular frequency ω_1) and a continuous-wave (c.w.) signal field (amplitude A_2 and angular frequency ω_2). The pump pulse train of maximum intra-waveguide peak powers at 11.7 W generates high free-carrier densities on the order of 10^{19} cm⁻³. The 50 MHz pulse repetition rate allows sufficient time (more than $40\tau_c$) for complete free-carrier recombination relaxation so that no inter-pulse interference occurs. Moreover, with the small waveguide dispersion and short waveguide length, the dispersion-induced linear phase mismatch $\Delta\phi$ is negligibly small within the examined 1550 nm to 1562 nm wavelength range: the maximum value of $\Delta\phi \times L$ is only 0.0037π , as shown in Fig. 1(c), which does not have appreciable impact on the wave-mixing process [25], [27]–[29].

Figure 1(d) shows two examples of the wave-mixing spectra generated in the silicon nanowire waveguide, with input laser detunings equal to ± 0.28 THz; the generated sidebands are denoted as s1 and s2, respectively. Here the input pulse peak power is 11.7 W and the c.w. power is 0.4 mW. Significantly, we observe that the output pulse spectra have an apparent FCD-induced spectral blue shift (~ 0.03 THz) [20]–[24], and the output c.w. spectra exhibit the feature of FCD-induced cross-phase modulation from the pulse [28]. Consequently, the generated wave-mixing idler spectra show complex and broadened structures. All these evidences indicate that the measured wave-mixing processes are conducted in a regime with strong nonlinear free-carrier dynamics. To confirm this, Fig. 1(e), upper panel, shows the numerically simulated wave-mixing spectrum using the NLSE model given by Eqs. (1) and (2), which illustrates remarkable agreement with the measurements without fitting. Meanwhile, we note that when the free-carrier dynamics is eliminated from the model, as shown in Fig. 1(e), lower panel, the modeled output spectra lose all the salient features (line-shape broadening, asymmetry, and spectral dips) observed in our measurements.

3.1. Inverse dependence of FC-SWM on input pump-signal laser detuning

From the expressions of parameters H and M in Eqs. (4) and (5), it is noted that the FC-SWM sideband power inversely depends on the input laser detuning ($1/b$). Intrinsically, the $1/b$ factor originates from the temporal integration of $|E|^4$ in the rate equation of carrier density N_c , that is, the slower beating oscillation between the input lasers gives rise to higher carrier density fluctuations, and potentially imposes larger six-wave-mixing strengths [14]. To demonstrate such dynamics, we scan the input laser detuning from -0.7 THz to 0.7 THz by changing the input c.w. frequency and record the wave-mixing sideband powers at each scan point, as shown in Fig. 2(a). Intriguingly, we observe that for the 11.7 W input pulse, as the input laser detuning changes

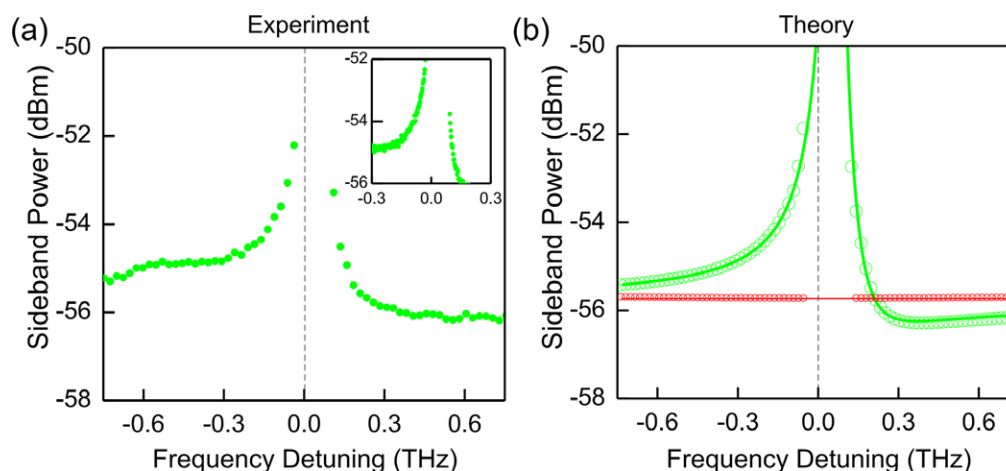


Figure 2 Direct detuning dependence of the Drude FC-SWM. (a) Experimentally measured wave-mixing sideband powers as a function of input laser detuning. The gap in the middle detuning arises because, in such region, the generated sideband components are covered by the pulse spectrum. The laser scanning step is 25 GHz. The inset shows more densely recorded data with 2.5 GHz step within the closer detuning window from -0.3 THz to 0.3 THz. (b) Numerical (open circles) and analytical (solid lines) wave-mixing sideband powers calculated as a function of laser detuning. The green circles and line are for FC-SWM and the red circles and line are for pure FWM (without the free-carrier contributions). To compare theory with experiment, the calculated sideband powers are down shifted by 23 dB to compensate for the 50 MHz pulse repetition rate and power attenuation in the measurement.

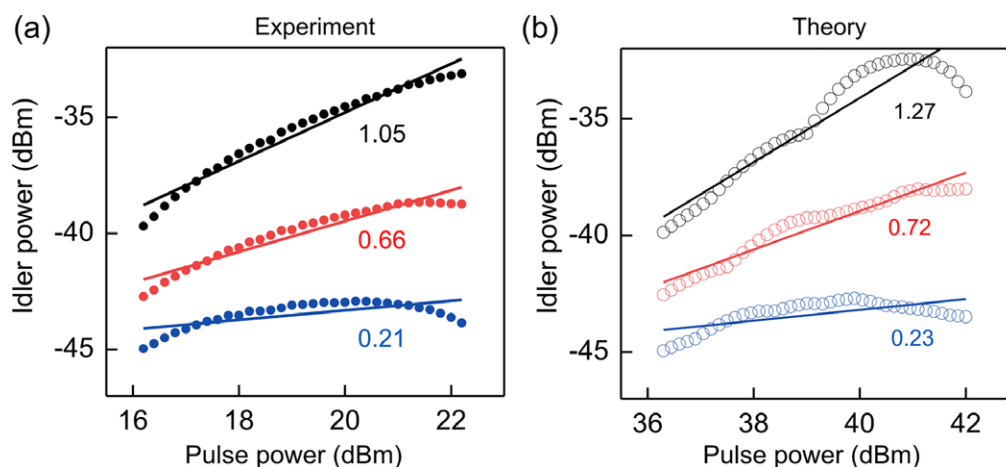


Figure 3 Strong dependences of FC-SWM on pump power. (a) Experimentally measured power transfer function between the input pulse and generated wave-mixing sideband, under three different detunings: 0.025 THz (black), 0.25 THz (red), and 1.25 THz (blue). The solid lines are linear fits of the experimental data, with the fitted slope coefficients listed below each corresponding line. (b) Numerically simulated power transfer functions corresponding to the results in panel (a).

from ± 0.3 THz to zero, the generated wave-mixing sideband power exhibits an increase of about 3.0 dB, clearly verifying the $1/b$ dependence prediction. To support the measurements, Fig. 2(b) shows the corresponding numerical simulation via the NLSE model of Eqs. (1) and (2), as well as the analytical calculation via Eq. (5), both achieving remarkable agreements with our measurements. For comparison, in Fig. 2(b) we plot the theoretical FWM sideband powers induced solely by the Kerr effect and TPA, which show no detuning dependence, and confirms that the waveguide dispersion is negligible compared to the intrinsic $1/b$ dependence of FC-SWM [25]. Particularly, it is seen from Fig. 2(b) that, when the laser detuning approaches zero,

FC-SWM becomes dominant over FWM (e.g., at 0.1 THz detuning, the FC-SWM sideband is -24.0 dBm, about 4.0 dB larger than FWM), strongly supporting the existence of FC-SWM in silicon.

3.2. Strong pump power dependency of FC-SWM

From Eq. (5) and the expressions of P , G , D , and A , the FWM strength caused by the third-order Kerr effect and TPA is proportional to $A_1 A_2$, while the FC-SWM strength

Table 1 Wave-mixing coefficients induced by different constituents of nonlinear processes.

Effects	NM_{-b}	NM_b
Kerr+TPA	$-MJ_0/2 + iJ_1$	$-MJ_0/2 + iJ_1$
TPA+FCA	$Me^{i\psi/2}$	$Me^{-i\psi/2}$
Kerr+FCD	$-J_1e^{-i\theta}$	$J_1e^{i\theta}$
FCA+FCD	$-iMJ_0/2 + J_1$	$iMJ_0/2 - J_1$
Kerr+FCA	$-iMJ_0/2 + iJ_1$	$iMJ_0/2 + iJ_1$
TPA+FCD	$-iMJ_0/2 + J_1$	$-iMJ_0/2 - J_1$

induced by FCD/FCA is proportional to $A_1^3 A_2$, rooting in the fifth-order nonlinear property of FC-SWM. To observe this higher pump power sensitivity of FC-SWM than FWM, Fig. 3(a) and (b) plot the experimental and theoretical power transfer functions between the input pulse peak power and the generated wave-mixing sideband power, under three different frequency detuning values: 0.025 THz, 0.25 THz, and 1.25 THz. Particularly, with the $1/b$ scaling of the FC-SWM demonstrated above, as the detuning decreases from 1.25 THz to 0.025 THz, the contribution of FC-SWM in the overall wave-mixing process is substantially enhanced. Simultaneously the slope (linearly fitted) of the power transfer function increases from 0.21 to 1.05, clearly illustrating the

stronger pump power dependence of FC-SWM over FWM. Ideally, the FC-SWM (FWM) produces a power transfer function with slope equal to 4 (2) [14], [15], but, with the concurrent existence of TPA and FCA, the pulse and c.w. laser fields are heavily attenuated in the nanowire waveguide [21], [22], and resultantly the measured and calculated power transfer functions are much less steep, as shown in Fig. 3(a) and (b). Even so, the power transfer function dominated by FC-SWM shows a $5\times$ slope improvement over solely FWM, further confirming the fifth-order nature of FC-SWM.

3.3. Phase-sensitive interaction between FC-SWM and FWM

It is observed from Fig. 2(a) and (b) that, with the utilized experimental parameters, FC-SWM and FWM coexist and have comparative magnitudes, which allows us to explore the interplay between six- and four-wave mixing in silicon. As illustrated in Eqs. (6) and (7), the combinational effect of FC-SWM and FWM produces an overall wave-mixing strength that is asymmetrical for positive and negative input laser detunings. Since the waveguide dispersion is neglected in the derivation, such unconventional asymmetry could arise from the interplay between FC-SWM and FWM [30], [31]. The same dynamics is observed

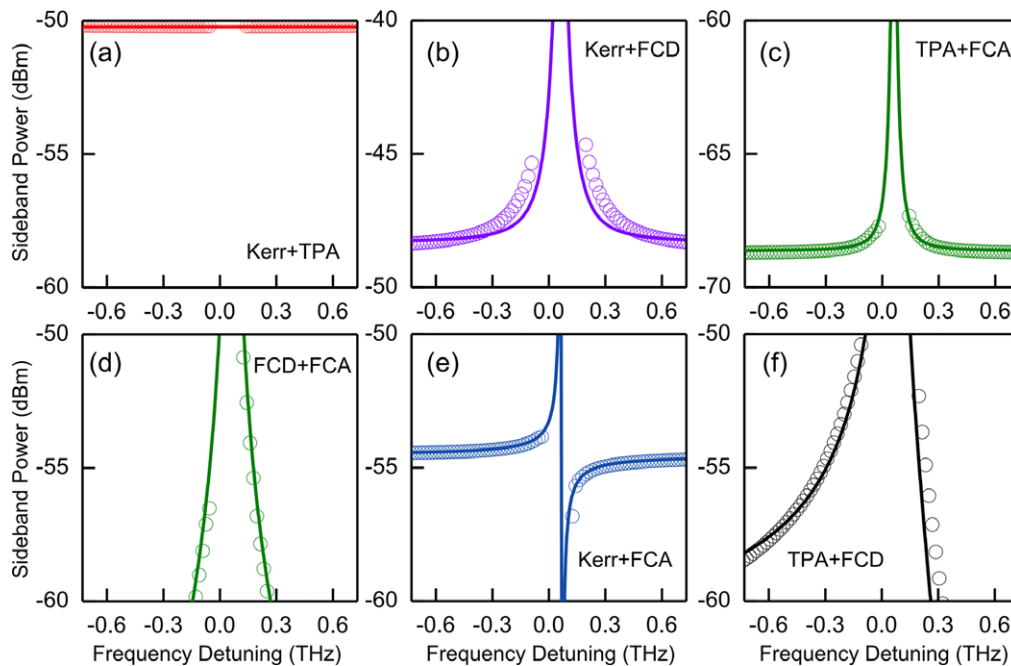


Figure 4 Comparative detuning line-shape symmetries and asymmetries for different nonlinear constituents, noted in Table 1. The open circles are from numerical NLSE simulation and the solid lines are from analytical calculations, based on parameters used from Fig. 2 at 11.7 W. (a) Solely Kerr and TPA without free-carrier dynamics, with negligible detuning dependences. (b) Kerr and FCD constituents, with symmetric line shape. (c) TPA and FCA constituents, with symmetric line shape. (d) FCD and FCA constituents, with symmetric line shape. (e) Kerr and FCA constituents, with line-shape asymmetry. (f) TPA and FCD constituents, with line-shape asymmetry. Note that the numerical results of the sideband powers close to zero detuning are subtracted due to the overlap with the pump spectra line width itself.

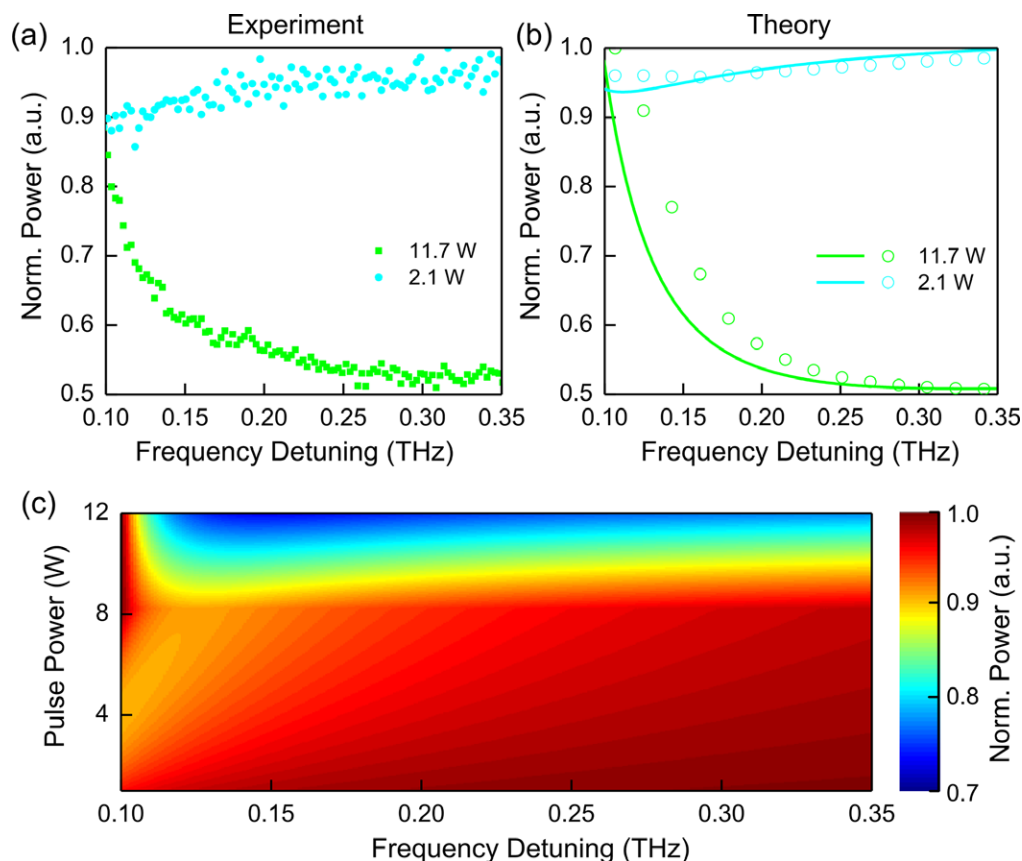


Figure 5 Wave-mixing evolution via the phase-sensitive superposition of FC-SWM and FWM. (a) Experimentally measured wave-mixing sideband powers as a function of input laser detuning, under two different input pulse peak powers: 11.7 W (green) and 2.1 W (cyan). The laser scanning resolution is 2.5 GHz. (b) Numerical (open circles) and analytical (solid lines) calculated wave-mixing sideband power evolution, corresponding to a 11.7 W and a 2.1 W pulse. (c) Calculated false-color image of overall wave-mixing sideband powers while sweeping input pulse powers from 1 W to 12 W. The sideband powers are normalized to the maximum value for each input pulse power.

experimentally in Fig. 1(d); for two opposite detuning values ± 0.28 THz, the generated power of sidebands s_1 and s_2 has an appreciable difference of 1.6 dB. More generally, as observed in Fig. 2(a), the recorded sideband powers exhibit as an apparently asymmetric line shape as the wavelength detunes from -0.70 THz to 0.70 THz.

To elucidate such unconventional sideband evolutions and probe the interaction between different nonlinear wave-mixing processes, we tailored Eqs. (6) and (7) with different sets of nonlinear process combinations. As summarized in Table 1, for TPA and FCD, Kerr, and FCA, we indeed obtain unequal wave-mixing intensity with $\pm b$ detuning; while the other combinations all generate symmetric sideband powers. Importantly, comparing Table 1 and Eq. (3), we conclude that the breaking of wave-mixing symmetry can only originate from the interplay between the nonlinear amplitude modulations and the nonlinear phase modulations that have a phase offset of $\pi/2$ (i.e., between TPA and FCD, Kerr, and FCA). Figure 4 shows the analytically calculated wave-mixing sideband powers as a function of detuning; the features predicted in Table 1 are clearly illustrated. To further confirm our analysis, Fig. 4 also presents

the numerically simulated sideband powers under different nonlinear effects in Eqs. (1) and (2), which agree very well with the analytical results.

Moreover, we find that the phase-sensitive interaction between FC-SWM and FWM significantly modifies the overall sideband generation and opens up new possibilities to manipulate the multi-wave energy exchange in silicon. As indicated in Eqs. (6) and (7), the contributions of FC-SWM and FWM are intertwined within the functions H , M , J_0 , and J_1 , which have different monotonicities. Hence, the change of each effect can result in variation of the overall sideband power evolution in a nonexplicit fashion. To demonstrate this, Fig. 5(a) and (b) show the measured and calculated sideband power evolution for two input pulse peak powers. Particularly, for the 11.7 W pulses, FC-SWM dominates FWM such that the sideband evolution approximately follows the $1/b$ dependence featured by FC-SWM, as discussed above in Fig. 2(a) and (b). On the other hand, when the input pulse power is decreased to 2.1 W, FC-SWM is subjected to more degradation due to its higher dependence on the pump power. Consequently, at this power level, FWM now competes with FC-SWM and

results in approximate independence of sideband power on detuning b , as shown in Fig. 5(a) and (b). More generally, Fig. 5(c) shows the calculated sideband power evolution while sweeping the input pulse power. We observe that as the pulse power increases from 1 W to 12 W, the sideband evolution changes significantly, providing abundant and readily accessible power transfer functions. Such coupled and controllable sideband evolutions can be applicable for all-optical signal processing applications such as all-optical signal regeneration and frequency conversion.

4. Conclusion

Here we report the original demonstrations and analysis of Drude free-carrier plasma-induced six-wave mixing in silicon nanowire waveguides. Unique features of FC-SWM have been experimentally observed and discussed in depth. First, the non-dispersion-induced inverse dependence of FC-SWM frequency conversion on the input laser detuning is observed, with FC-SWM sideband power rapidly increasing by 3.0 dB within a 0.3 THz detuning window. Second, the strong dependence of the FC-SWM on input pump powers is illustrated. Third, the phase-sensitive interaction between FC-SWM and FWM is demonstrated for the first time, giving rise to the asymmetric line shape of sideband power evolution as a function of laser detuning. These observations not only advance our understanding of free-carrier nonlinear dynamics in the multiple-wave regime, but also open up new possibilities for applications based on wave mixing, such as on-chip spectral broadening and all-optical signal processing. Finally, the processes and phenomena demonstrated here can potentially be observed in other physical systems involving plasma nonlinearity, such as gas photo-ionization in hollow-core photonic crystal fibers [32]–[34] and light–plasma interactions in semiconductor photonic crystals [35].

Supporting Information

Additional supporting information may be found in the online version of this article at the publisher's website.

Acknowledgements. This work was funded by the China 863 Grant 2013AA014402, UESTC Young Faculty Award ZYGX2015-KYQD051, NSF CBET-1438147 and DMR-1611598, Air Force Office of Scientific Research Young Investigator Award (S. W. Huang) FA9550-15-1-0081, and Office of Naval Research N00014-14-1-0041. The authors acknowledge discussions with Xingyu Zhou, Feng Wen, Baojian Wu, and Jinghui Yang.

Received: 14 May 2016, **Revised:** 13 August 2016,

Accepted: 29 August 2016

Published online: 3 October 2016

Key words: silicon nanowire waveguide, free-carrier nonlinearity, four-wave mixing, six-wave mixing.

References

- [1] M. A. Foster, A. C. Turner, J. E. Sharping, B. S. Schmidt, M. Lipson, and A. L. Gaeta, *Nature* **441**, 960 (2006).
- [2] I. C. Khoo, R. Normandin, T. H. Liu, R. R. Michael, and R. G. Lindquist, *Phys. Rev. B* **40**, 7759 (1989).
- [3] H. Fukuda, K. Yamada, T. Shoji, M. Takahashi, T. Tsuchizawa, T. Watanabe, J. Takahashi, and S. Itabashi, *Opt. Express* **13**, 4629 (2005).
- [4] M. Dinu, F. Quochi, and H. Garcia, *Appl. Phys. Lett.* **82**, 2954 (2003).
- [5] J. F. McMillan, M. Yu, D. L. Kwong, and C. W. Wong, *Opt. Express* **18**, 15484 (2010).
- [6] R. Salem, M. A. Foster, A. C. Turner, D. F. Geraghty, M. Lipson, and A. L. Gaeta, *Nat. Photon.* **2**, 35 (2008).
- [7] S. Zlatanovic, J. S. Park, S. Moro, J. M. C. Boggio, I. B. Divliansky, N. Alic, S. Mookherjea, and S. Radic, *Nat. Photon.* **4**, 561 (2010).
- [8] X. Liu, R. M. Osgood, Y. A. Vlasov, and W. M. J. Green, *Nat. Photon.* **4**, 557 (2010).
- [9] M. A. Foster, R. Salem, D. F. Geraghty, A. C. Turner-Foster, M. Lipson, and A. L. Gaeta, *Nature* **456**, 81 (2008).
- [10] L. Zhang, Q. Lin, Y. Yue, Y. Yan, R. G. Beausoleil, and A. E. Willner, *Opt. Express* **20**, 1685 (2012).
- [11] T. Gu, N. Petrone, J. F. McMillan, A. van der Zande, M. Yu, G. Q. Lo, D. L. Kwong, J. Hone, and C. W. Wong, *Nat. Photon.* **6**, 554 (2012).
- [12] J. E. Sharping, K. F. Lee, M. A. Foster, A. C. Turner, B. S. Schmidt, M. Lipson, A. L. Gaeta, and P. Kumar, *Opt. Express* **14**, 12388 (2006).
- [13] C. Voelkmann, M. Reichelt, T. Meier, S. W. Koch, and U. Hofer, *Phys. Rev. Lett.* **92**, 127405 (2004).
- [14] Q. Lin, O. J. Painter, and G. P. Agrawal, *Opt. Express* **15**, 16604 (2007).
- [15] G. P. Agrawal, *Nonlinear Fiber Optics* (Academic Press, New York, 2001), p. 111.
- [16] A. Blanco-Redondo, D. Eades, J. Li, S. Lefrancois, T. F. Krauss, B. J. Eggleton, and C. Husko, *Optica* **1**, 299 (2014).
- [17] S. Lefrancois, C. Husko, A. Blanco-Redondo, and B. J. Eggleton, *J. Opt. Soc. Am. B* **32**, 218 (2015).
- [18] C. Husko, M. Wulf, S. Lefrancois, S. Combri, G. Lehoucq, A. De Rossi, B. J. Eggleton, and L. Kuipers, *Nat. Commun.* **7**, 11332 (2016).
- [19] Q. Lin, J. Zhang, P. M. Fauchet, and G. P. Agrawal, *Opt. Express* **14**, 4786 (2006).
- [20] A. B. Redondo, C. Husko, D. Eades, Y. Zhang, J. Li, T. F. Krauss, and B. J. Eggleton, *Nat. Commun.* **5**, 3160 (2014).
- [21] P. Colman, S. Combri, G. Lehoucq, A. De Rossi, and S. Trillo, *Phys. Rev. Lett.* **109**, 093901 (2012).
- [22] X. Yang and C. W. Wong, *Opt. Express* **15**, 4763 (2007).
- [23] C. Monat, B. Corcoran, D. Pudo, M. Heidari, C. Grillet, M. D. Pelusi, D. J. Moss, B. J. Eggleton, T. P. White, L. OFaolain, and T. F. Krauss, *IEEE J. Sel. Top. Quantum Electron.* **16**, 344 (2010).
- [24] S. Roy, A. Marini, and F. Biancalana, *Phys. Rev. A* **87**, 065803 (2013).
- [25] H. Zhou, M. Liao, S. W. Huang, L. J. Zhou, K. Qiu, and C. W. Wong, *Laser Photon. Rev.* **1**, 1111 (2016). See online supporting information.

- [26] M. Schultze, K. Ramasesha, C. D. Pemmaraju, S. A. Sato, D. Whitmore, A. Gandman, J. S. Prell, L. J. Borja, D. Prendergast, K. Yabana, D. M. Neumark, and S. R. Leone, *Science* **346**, 1348 (2014).
- [27] M. Erkintalo, Y. Q. Xu, S. G. Murdoch, J. M. Dudley, and G. Genty, *Phys. Rev. Lett.* **109**, 223904 (2012).
- [28] I. W. Hsieh, X. G. Chen, J. Dadap, N. Panoiu, R. Osgood, S. McNab, and Y. Vlasov, *Opt. Express* **15**, 1135 (2007).
- [29] D. Dimitropoulos, V. Raghunathan, R. Claps, and B. Jalali, *Opt. Express* **12**, 149 (2003).
- [30] Y. P. Zhang, A. W. Brown, and M. Xiao, *Phys. Rev. Lett.* **99**, 123603 (2007).
- [31] Y. P. Zhang, U. Khadka, B. Anderson, and M. Xiao, *Phys. Rev. Lett.* **102**, 013601 (2009).
- [32] M. F. Saleh, W. Chang, P. Hoelzer, A. Nazarkin, J. C. Travers, N. Y. Joly, P. St. J. Russell, and F. Biancalana, *Phys. Rev. Lett.* **107**, 203902 (2011).
- [33] M. F. Saleh, W. Chang, J. C. Travers, P. St. J. Russell, and F. Biancalana, *Phys. Rev. Lett.* **109**, 113902 (2012).
- [34] D. Novoa, M. Cassataro, J. C. Travers, and P. St. J. Russell, *Phys. Rev. Lett.* **115**, 203902 (2011).
- [35] C. A. Husko, S. Combri, P. Colman, J. Zheng, A. De Rossi, and C. W. Wong, *Sci. Rep.* **3**, 1100 (2013).

Supporting Information: Six-wave mixing induced by free-carrier plasma in silicon nanowire waveguides

Heng Zhou^{1,*}, Mingle Liao¹, Shu-Wei Huang², Linjie Zhou³, Kun Qiu¹ and Chee Wei Wong^{2,*}

¹ Key Lab of Optical Fiber Sensing and Communication Networks, University of Electronic Science and Technology of China, Chengdu 611731, China.

² Mesoscopic Optics and Quantum Electronics Laboratory, University of California, Los Angeles, CA 90095, USA.

³ State Key Laboratory of Advanced Optical Communication Systems and Networks, Shanghai Jiao Tong University, Shanghai 200240, China.

*Corresponding author: zhouheng@uestc.edu.cn; cheewei.wong@ucla.edu

I. Configuration of the experimental measurements

In this study we examine six-wave mixing caused by the effective $\chi^{(5)}$ free-carrier plasma nonlinear dynamics. To demonstrate six-wave mixing, the most intuitive way is to apply five different input frequencies and reveal the non-degenerate wave mixing sidebands. However, as discussed in the main text, FC-SWM and FWM concurrently takes place in silicon nanowire; and a six-wave mixing process can always be decomposed into two cascaded four-wave mixing processes [R1]. In other words, the sideband frequencies generated by FC-SWM are always overlapped with cascaded FWMs – thus we cannot distinguish them simply by sideband frequencies [R2]. On such basis, in this Letter we utilized a two-laser experiment configuration to study degenerate FWM and degenerate FC-SWM processes (as shown in Fig. S1), and unambiguously demonstrate the existence of FC-SWM by discovering the regime where FC-SWM sufficiently prevails over FWM, caused intrinsically by the direct detuning dependence of FC-SWM, as shown in Fig. 2 of the main text. Furthermore, such compact and efficient experiment configuration also greatly simplifies the theoretical derivation towards the concise expressions of wave mixing sideband coefficients shown in Eq. (5-7) of the main text, which greatly facilitates our analysis of this nonlinear phenomenon.

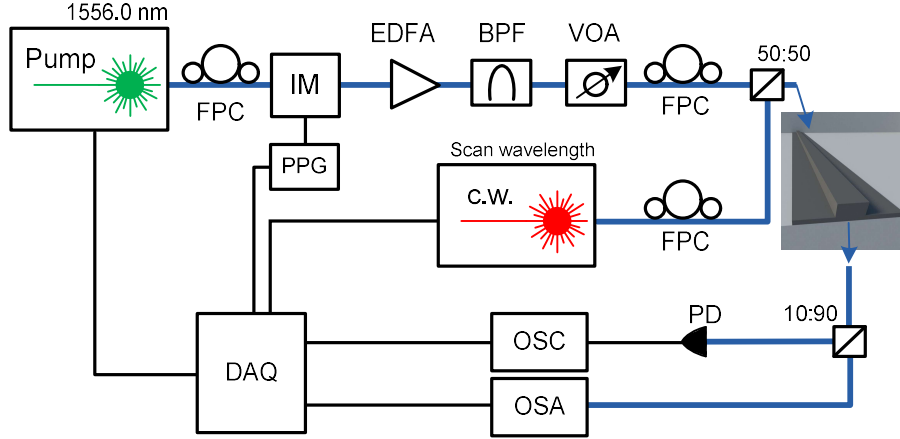


FIG. S1. Schematics of the experiment setup. FPC: fiber polarization controller, IM: intensity modulator; PPG: pulse-pattern generator; EDFA: erbium-doped fiber amplifier; BPF: band-pass filtering; VOA: variable optical attenuator; PD: photon diode; OSC: Oscilloscope; OSA: optical spectrum analyzer; and DAQ: data acquisition.

II. Derivation of the nonlinear modulation coefficient

The nonlinear field dynamics in the silicon nanowire is described by the nonlinear Schrödinger equation (NLSE) coupled with the rate equation of the intra-nanowire free-carrier density $N_c(z, t)$, given by [R3-R5]:

$$\frac{\partial E}{\partial z} = -i \frac{\beta_2}{2} \frac{\partial^2 E}{\partial t^2} + \frac{\beta_3}{6} \frac{\partial^3 E}{\partial t^3} - \frac{\alpha_l}{2} E + (i\gamma_{eff} - \frac{\beta_{TPA}}{2A_0}) |E|^2 E - (i\delta + \sigma) N_c E \quad (S1)$$

$$N_c(z, t) = \int_0^t \left(\frac{\beta_{TPA}}{2A_0^2 h\nu_0} |E(z, \tau)|^4 - \frac{N_c(z, \tau)}{\tau_c} \right) d\tau \quad (S2)$$

In Eq. (S1-S2), E is the slowly-varying envelope of the intra-nanowire electromagnetic fields, β_n is the n th order dispersion, α_l is the linear loss, γ_{eff} is the effective Kerr nonlinear coefficient, β_{TPA} is the degenerate two-photon absorption (TPA) coefficient, δ and σ is the free-carrier dispersion (FCD) and free-carrier absorption (FCA) coefficient respectively, A_0 is the effective mode area, and τ_c is the free-carrier lifetime. $N_c(z, t)$ is the free-carrier density with explicit z - and t -dependences shown for clarity. To study the wave mixing processes, we assume that, without loss of generality, an incident light field onto the silicon nanowire as $E = A_1 \cos(\omega_1 t) + A_2 \cos(\omega_2 t)$. To facilitate comparison with our measurements, here A_1 is a quasi-square pulse envelope with pulsewidth at half-maximum equal to T_o , and $A_1 \gg A_2$.

Examining the evolution of the overall input fields and neglecting the small nanowire dispersion, the nonlinear modulation term (NM) experienced by the input fields in the nanowire can be described by:

$$NM = \exp\left(L\left(i\gamma_{eff} - \frac{\beta_{TPA}}{2A_0}\right)|E|^2 - \frac{L(i\delta + \sigma)\beta_{TPA}}{2A_0^2 h\nu_0} \int_0^t |E|^4 dt\right) \quad (S3)$$

Here L is the nanowire length. In Eq. (S3) we neglect free-carrier recombination relaxation since it is much slower (\sim ns to 250 ps) than the beating oscillations considered in our study ($2\pi\tau_c \gg (\omega_1 - \omega_2)^{-1}$). With the slow-varying envelope approximation [R1], we can neglect those fast oscillations at frequencies ω_1, ω_2 , as well as their summation and multiples. Hence one obtains:

$$|E|^2 \rightarrow \frac{A_1^2}{2} + A_1 A_2 \cos(\omega_1 t - \omega_2 t) \quad (S4)$$

$$\begin{aligned} |E|^4 &\rightarrow A_1^4 \cos^4(\omega_1 t) + 4A_1^3 A_2 \cos^3(\omega_1 t) \cos(\omega_2 t) \\ &\rightarrow \frac{3A_1^4}{8} + \frac{3A_1^3 A_2}{2} \cos(\omega_1 t - \omega_2 t) \end{aligned} \quad (S5)$$

In the above derivation we use the condition that $A_1 \gg A_2$, relevant for our measurements, and neglect the terms containing A_2^2 . Considering that NM eventually applies on the high power pulse field $A_1 \cos(\omega_1 t)$, Eq. (S4) represents the four-wave mixing process $\chi^{(3)}(2\omega_1 - \omega_2; \omega_1, \omega_1, \omega_2)$ and Eq. (S5) represents the six-wave mixing process $\chi_{FC}^{(5)}(2\omega_1 - \omega_2; \omega_1, \omega_1, -\omega_1, \omega_1, \omega_2)$. It is seen that under our experimental configuration, particular wave interactions are different for four- and six-wave mixing but both result in nonlinear modulation of frequency $\omega_1 - \omega_2$. Substituting Eq. (S4-S5) into Eq. (S3), we obtain:

$$NM = \exp\left(L\left(i\gamma_{eff} - \frac{\beta_{TPA}}{2A_0}\right)\left(\frac{A_1^2}{2} + A_1 A_2 \cos(bt)\right) - \frac{(i\delta + \sigma)\beta_{TPA}L}{2A_0^2 h\nu_0} \left(\frac{3A_1^4 T_0}{8} + \frac{3A_1^3 A_2}{2b} \sin(bt)\right)\right) \quad (S6)$$

where $b = \omega_1 - \omega_2$. To focus on the wave mixing processes, we eliminate the constant modulation terms in Eq. (S6) and keep only the oscillation terms to obtain:

$$NM = \exp\left(\left(iG + P\right)\cos(bt) + \frac{(iD + A)}{b}\sin(bt)\right) \quad (S7)$$

Here $G = LA_1A_2\gamma_{\text{eff}}$, $P = -LA_1A_2\beta_{\text{TPA}}(2A_0)^{-1}$, $D = -3LA_1^3A_2\delta\beta_{\text{TPA}}(4A_0^2h\nu_0)^{-1}$, $A = D\sigma\delta^{-1}$. With our experimental parameters, we find that G, P, D, A are each substantially smaller than 1, such that Eq. (S3) is simplified to:

$$NM = \exp(iG \cos(bt) + \frac{iD}{b} \sin(bt)) \times (1 + P \cos(bt)) \times (1 + \frac{A}{b} \sin(bt)) \quad (\text{S8})$$

Eq. (S8) can be further rearranged into the following form:

$$NM = \exp(iH \sin(bt + \theta)) \times (1 + M \cos(bt + \psi)) \quad (\text{S9})$$

where $H = \sqrt{(D/b)^2 + G^2}$, $M = \sqrt{(A/b)^2 + P^2}$, with $\theta = \arctan(Gb/D)$, $\pi/2 \leq \theta < \pi$, and $\psi = \arctan(-A/Pb)$, $\pi/2 \leq \psi < \pi$. The values of θ and ψ are determined by the signs of G, P, D , and A . Using the Bessel expansion and Euler's formula, we obtain:

$$NM = \sum_{n=-1}^1 J_n(H) e^{inbt+in\theta} \times \left(1 + \frac{1}{2} M (e^{ibt+i\psi} + e^{-ibt-i\psi}) \right). \quad (\text{S10})$$

Here J_n is the n th order Bessel function. In Eq. (S10) we note that the only possible values of n are -1, 0, and 1 because phase-matching condition cannot be satisfied for higher eigenfrequencies as confirmed in the measurements. Subsequently, the nonlinear modulation terms at opposite detunings $\pm b$ are:

$$NM_b = \frac{1}{2} MJ_0 e^{i\psi} + J_1 e^{i\theta} \quad (\text{S11})$$

$$NM_{-b} = \frac{1}{2} MJ_0 e^{-i\psi} - J_1 e^{-i\theta} \quad (\text{S12})$$

In the above derivation we used $J_{-1} = -J_1$.

III. Deriving the interactions between different nonlinear six-wave and four-wave mixing effects

Below is the detailed derivation of Table I in the main text, based on Eq. (S11-S12).

- i.* when only Kerr and TPA are applied, $A=0, D=0, \theta = \pi/2, \psi = \pi, NM_b = -MJ_0/2 + iJ_1;$
 $NM_{-b} = -MJ_0/2 + iJ_1.$
- ii.* when only TPA and FCA are applied, $D=0, G=0, NM_b = Me^{i\varphi}/2; NM_{-b} = Me^{-i\varphi}/2.$
- iii.* when only Kerr and FCD are applied, $A=0, P=0, NM_b = J_1 e^{i\theta}; NM_{-b} = -J_1 e^{-i\theta}.$
- iv.* when only FCA and FCD are applied, $G=0, P=0, \theta = \pi, \psi = 3\pi/2, NM_b = iMJ_0/2 - J_1;$
 $NM_{-b} = -MJ_0/2 + J_1.$

- v. when only Kerr and FCA are applied, $P=0, D=0, \theta = \pi/2, \psi = 3\pi/2, NM_b = iMJ_0/2 + iJ_1;$
 $NM_{-b} = -iMJ_0/2 + iJ_1.$
- vi. when only FCD and TPA are applied, $G=0, A=0, \theta = \pi, \psi = \pi, NM_b = -MJ_0/2 - J_1;$
 $NM_{-b} = -MJ_0/2 + J_1.$

IV. Comparing the analytical results with experimental and numerical results

To connect Eq. (S11-S12) with the experimental results shown in Fig. 1 in the main text, the wave mixing sideband s_1 generated at $\omega_l - b$ corresponds to NM_b [S5], and its power can be written as:

$$P_{s1} = \left| \left(\frac{1}{2} MJ_0 e^{i\psi} + J_1 e^{i\theta} \right) A_1 \right|^2 \quad (\text{S13})$$

Similarly, the wave mixing sideband s_2 generated at $\omega_l + b$ corresponds to NM_{-b} , and its power can be written as:

$$P_{s2} = \left| \left(\frac{1}{2} MJ_0 e^{-i\psi} - J_1 e^{-i\theta} \right) A_1 \right|^2 \quad (\text{S14})$$

In deriving of the above equations, we neglected nanowire dispersion and the time-independent nonlinear phase-shift induced by Kerr SPM, XPM, and FCD, which can in turn cause phase mismatch and reduce the sideband generation in the wave mixing process. However, we note that: i) the nanowire dispersion is comparatively negligibly small in our study; and ii) the overall phase mismatch caused by the nonlinear phase shift is independent of detuning. Therefore, there is only a constant discrepancy (~ 4 dB) between the sideband powers predicted by Eq. (S13-S14) and the experimental sideband measurements (and numerical simulated sideband powers). Correcting for this constant offset, the analytical results are nicely in line with simulations and experiments, as shown in Fig. 2 and Fig. 4 of the main text. Also, Fig. in the main text compares the numerical and analytical results induced by each combination of nonlinear wave mixing effects as listed in Table I in the main text, all exhibiting favorable agreement with each other.

V. Coupled-mode equations containing FC-SWM

Here we derive the coupled-mode equations of wave mixing in the presence of FC-SWM, based on the configuration adopted in our experiment [R6-R8]. Substituting the overall intra-nanowire field $E = E_1 + E_2 + E_3 = A_1 \cos(\omega_1 t) + A_2 \cos(\omega_2 t) + A_3 \cos(\omega_3 t)$ into Eq. (S1-S2) and following the derivation of Eq. (S6), we obtain:

$$dE = \left(\left(i\gamma_{eff} + \frac{\beta_{TPA}}{2A_0} \right) \left(\frac{A_1^2}{2} + A_1 A_2 \cos(bt) + A_1 A_3 \cos(bt) \right) + \frac{(i\delta + \sigma)\beta_{TPA}}{2A_0^2 h\nu_0} \left(\frac{3A_1^4 T_0}{8} + \frac{3A_1^3 A_2}{2b} \sin(bt) + \frac{3A_1^3 A_3}{2b} \sin(bt) \right) \right) \times \frac{dz}{L} E \quad (S15)$$

Expanding Eq. (S15) and gathering the terms with eigenfrequency ω_1 , ω_2 and $\omega_3 = \omega_1 - \omega_2$, we have:

$$\frac{dA_1}{dz} = \left(\left(i\gamma_{eff} + \frac{\beta_{TPA}}{2A_0} \right) |A_1|^2 + \frac{3(i\delta + \sigma)\beta_{TPA}}{16A_0^2 h\nu_0} |A_1|^4 T_0 \right) A_1 \quad (S16)$$

$$\frac{dA_2}{dz} = \left(i\gamma_{eff} + \frac{\beta_{TPA}}{2A_0} \right) 2|A_1|^2 A_2 + \frac{3(i\delta + \sigma)\beta_{TPA}}{16A_0^2 h\nu_0} \left(|A_1|^4 T_0 + \frac{2|A_1|^2 A_1^2 e^{-i\frac{\pi}{2}}}{b} \right) A_2 \quad (S17)$$

$$\frac{dA_3}{dz} = \left(i\gamma_{eff} + \frac{\beta_{TPA}}{2A_0} \right) \left(2|A_1|^2 A_3 + A_1^2 A_2 \right) + \frac{3(i\delta + \sigma)\beta_{TPA}}{16A_0^2 h\nu_0} \left(\left(T_0 |A_1|^4 + \frac{2|A_1|^2 A_1^2 e^{-i\frac{\pi}{2}}}{b} \right) A_3 + \frac{2|A_1|^4 A_2 e^{-i\frac{\pi}{2}}}{b} \right) \quad (S18)$$

Here, in the derivation, we use $A_1 \gg A_2 \gg A_3$. Qualitatively, the pulse field E_1 experiences self-induced Kerr SPM, TPA, FCA, and FCD. The continuous-wave field E_2 mainly experiences Kerr XPM and the cross-induced TPA, FCA, and FCD from E_1 . The sideband field E_3 experiences XPM and the cross-induced TPA, FCA, and FCD from E_1 . Additionally it acquires energy from E_1 and E_2 via FWM (4th term in the RHS of Eq. (S18)) and FC-SWM (last term in the RHS of Eq. (S18)). The coupled-mode equation model illustrates the evolution of each wave participating in the wave mixing and, specifically it enables the modeling of the wave mixing phase matching dynamics, as described in the next Section.

VI. Phase matching consideration of FC-SWM

It can be seen from Eq. (S5) that the phase-matching condition for FC-SWM is $2\kappa_{\omega_1} - \kappa_{\omega_2} = \kappa_{\omega_3}$, where κ_{ω_i} is the propagation constant at wavelength ω_i . It is noted that although FC-SWM is a six-wave mixing processes, its phase-matching condition is identical with Kerr FWM, since we utilized the bichromatic laser input to study the degenerate FC-SWM ($\chi^{(5)}(2\omega_1 - \omega_2; \omega_1, \omega_1, -\omega_1, \omega_1, \omega_2)$) and FWM ($\chi^{(3)}(2\omega_1 - \omega_2; \omega_1, \omega_1, \omega_2)$) [R9-R10]. From Eq. (S16-S18), the phase mismatch can be written as:

$$\Delta\kappa = 2\kappa_{\omega_1} - \kappa_{\omega_2} - \kappa_{\omega_3} = \Delta\phi - 2\gamma_{eff} |A_1|^2 \quad (S19)$$

where $\Delta\phi$ denotes dispersion induced linear phase mismatch and $2\gamma_{eff} |A_1|^2$ denotes nonlinear phase mismatch caused by Kerr phase modulation. We emphasize that, as seen from Eq. (S16-S18), FCD causes large but identical nonlinear phase shift to all the intra-nanowire fields (as confirmed by the prominent spectral blue-shift and broadening of the pulse, c.w., and sideband spectrum shown in Fig. 1(b) of the main text), such that FCD does not contribute to the overall phase mismatch [R4, R11-R12]. Moreover, Fig. S2 shows the evolution of $\Delta\kappa \times L$ and the analytically calculated sideband power as the function of input laser wavelength detuning. We see that the peak value of $\Delta\kappa \times L$ is small ($\sim 0.34\pi$), implying that the experimentally demonstrated wave mixing operates close to phase matching condition. In addition, for the experimental nanowire as noted in the main text, the influence of the detuning dependent phase mismatch caused by dispersion ($\Delta\phi \times L \sim 0.0041\pi$) is substantially weaker than the intrinsic $1/b$ scaling of FC-SWM.

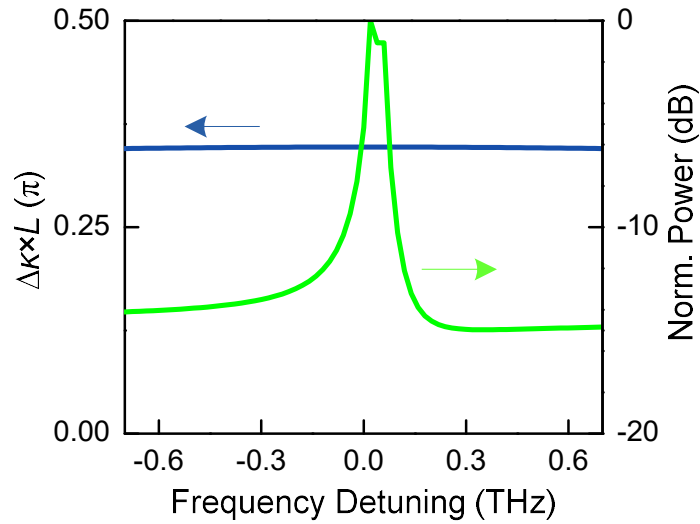


FIG. S2. Evolution of phase mismatch (left y-axis) and the analytically calculated normalized sideband power (right y-axis) as a function of input laser frequency detuning.

Supplementary References

- [R1] M. Erkintalo, Y. Q. Xu, S. G. Murdoch, J. M. Dudley, and G. Genty, “Cascaded phase matching and nonlinear symmetry breaking in fiber frequency combs,” *Phys. Rev. Lett.* **109**, 223904 (2012).
- [R2] Y. P. Zhang, U. Khadka, B. Anderson, M. Xiao, “Temporal and spatial interference between four-wave mixing and six-wave mixing channels,” *Phys. Rev. Lett.* **102**, 013601 (2009).

- [R3] X. Yang and C. W. Wong, “Coupled-mode theory for stimulated Raman scattering in high- Q/V_m silicon photonic band gap defect cavity lasers”, *Opt. Express* **15**, 4763 (2007).
- [R4] A. B. Redondo, C. A. Husko, D. Eades, Y. Zhang, J. Li, T. F. Krauss, and B. J. Eggleton, “Observation of soliton compression in silicon photonic crystals”, *Nat. Commun.* **5**, 3160 (2014).
- [R5] L. Yin and G. P. Agrawal, “Impact of two-photon absorption on self-phase modulation in silicon waveguides”, *Opt. Lett.* **32**, 2031 (2007).
- [R6] H. A. Haus, *Waves and fields in optoelectronics*, Prentice Hall, Englewood Cliffs, New Jersey, 1st edition, 1984.
- [R7] G. P. Agrawal, *Nonlinear Fiber Optics*, Academic Press, New York, New York, 3rd edition, 2001.
- [R8] Q. Lin, O. J. Painter, and G. P. Agrawal, “Nonlinear optical phenomena in silicon waveguides: Modeling and applications,” *Opt. Express* **15**, 16604 (2007).
- [R9] Q. Lin., J. Zhang, P. M. Fauchet, and G. P. Agrawal, “Ultrabroadband parametric generation and wavelength conversion in silicon waveguides”, *Opt. Express* **14**, 4786 (2006).
- [R10] D. Dimitropoulos, V. Raghunathan, R. Claps, and B. Jalali, “Phase-matching and nonlinear optical processes in silicon waveguides”, *Opt. Express* **12**, 149 (2003).
- [R11] C. Monat, B. Corcoran, D. Pudo, M. Heidari, C. Grillet, M. D. Pelusi, D. J. Moss, B. J. Eggleton, T. P. White, L. O’Faolain, and T. F. Krauss, “Slow light enhanced nonlinear optics in silicon photonic crystal waveguides”, *IEEE J. Sel. Topics Quantum Electron.* **16**, 344 (2010).
- [R12] S. Roy, A. Marini, and F. Biancalana, “Self-frequency blueshift of dissipative solitons in silicon-based waveguides”, *Phys. Rev. A* **87**, 065803 (2013).